# Valley-polarized nematic order in twisted moiré systems: In-plane orbital magnetism and non-Fermi liquid to Fermi liquid crossover

Ipsita Mandal
*Institute of Nuclear Physics, Polish Academy of Sciences, 31-342 Kraków, Poland*
*Department of Physics, Stockholm University, AlbaNova University Center, 106 91 Stockholm, Sweden*

Rafael M. Fernandes
*School of Physics and Astronomy, University of Minnesota, Minneapolis, Minnesota 55455, USA*

arXiv:2202.04630v3 [cond-mat.str-el] 17 Mar 2023

The interplay between strong correlations and non-trivial topology in twisted moiré systems can give rise to a rich landscape of ordered states that intertwine the spin, valley, and charge degrees of freedom. In this paper, we investigate the properties of a system that displays long-range valley-polarized nematic order. Besides breaking the threefold rotational symmetry of the triangular moiré superlattice, this type of order also breaks twofold rotational and time-reversal symmetries, which leads to interesting properties. First, we develop a phenomenological model to describe the onset of this ordered state in twisted moiré systems, and to explore its signatures in their thermodynamic and electronic properties. Its main manifestation is that it triggers the emergence of in-plane orbital magnetic moments oriented along high-symmetry lattice directions. We also investigate the properties of the valley-polarized nematic state at zero temperature. Due to the existence of a dangerously irrelevant coupling $\lambda$ in the six-state clock model that describes the putative valley-polarized nematic quantum critical point, the ordered state displays a pseudo-Goldstone mode. Using a two-patch model, we compute the fermionic self-energy to show that down to very low energies, the Yukawa-like coupling between the pseudo-Goldstone mode and the electronic degrees of freedom promotes the emergence of non-Fermi liquid behaviour. Below a crossover energy scale $\Omega^* \sim \lambda^{3/2}$, however, Fermi liquid behaviour is recovered. Finally, we discuss the applicability of these results to other non-trivial nematic states, such as the spin-polarized nematic phase.

## CONTENTS

I. Introduction 1

II. Valley-polarized nematic order in TBG 2
A. Phenomenological model 2
B. Manifestations of the valley-polarized phase 3
C. Impact of the valley-polarized order on the electronic spectrum 4

III. Pseudo-Goldstone modes in the valley-polarized nematic phase at zero temperature 4

IV. Non-Fermi liquid to Fermi liquid crossover 6
A. The patch model 6
B. Electronic self-energy 7
C. Hertz-Millis approach 9

V. Discussion and conclusions 10

Acknowledgments 11

References 11

## I. INTRODUCTION

The observation of electronic nematicity in the phase diagrams of twisted bilayer graphene [1–4] and twisted double-bilayer graphene [5, 6] provides a new setting to elucidate these electronic liquid crystalline states, which spontaneously break the rotational symmetry of the system. Shortly after nematicity was proposed to explain certain properties of high-temperature superconductors [7], it was recognized that the Goldstone mode of an ideal electronic nematic phase would have a profound impact on the electronic properties of a metal [8–10]. This is because, in contrast to other Goldstone modes such as phonons and magnons, which couple to the electronic density via a gradient term, the nematic Goldstone mode displays a direct Yukawa-like coupling to the electronic density [11]. As a result, it is expected to promote non-Fermi liquid (NFL) behaviour, as manifested in the sub-linear frequency dependence of the imaginary part of the electronic self-energy [8, 12].

However, because the crystal lattice breaks the continuous rotational symmetry of the system, the electronic nematic order parameter realized in layered quantum materials has a discrete $Z_q$ symmetry, rather than the continuous XY (or O(2)) symmetry of its two-dimensional (2D) liquid crystal counterpart [13]. In the square lattice, the $Z_2$ (Ising-like) symmetry is associated with selecting one of the two orthogonal in-plane directions, connecting either nearest-neighbor or next-nearest-neighbor sites [14]. In the triangular lattice, the $Z_3$ (three-state Potts/clock) symmetry refers to choosing one of the three bonds connecting nearest-neighbor sites [15, 16]. In both cases, the excitation spectrum in the ordered state is gapped, i.e. there is no nematic Goldstone mode. Consequently, NFL behaviour is not expected to arise inside the nematic phase — although it can still emerge in the disordered state due to interactions mediated by possible quantum critical fluctuations [17–27].

In twisted moiré systems [28, 29], which usually display an emergent triangular moiré superlattice, another type of nematic order can arise due to the presence of the valley degrees of freedom: a *valley-polarized nematic state* [30]. Compared with the standard nematic state, valley-polarized nematic order breaks not only the threefold rotational symmetry of the lattice, but also "inversion" (more

precisely, two-fold rotational), and time-reversal symmetries. It is another example, particularly relevant for moiré superlattices, of a broader class of "non-standard" electronic nematic orders that are intertwined with additional symmetries of the system, such as the so-called nematic spin-nematic phases [31–33].

In twisted bilayer graphene (TBG) [34–37], while threefold rotational symmetry-breaking [1–4] and time-reversal symmetry-breaking [37–40] have been observed in different regions of the phase diagram, it is not clear yet whether a valley-polarized nematic state is realized. Theoretically, the valley-polarized nematic order parameter has a $Z_6$ symmetry, which corresponds to the six-state clock model [41]. Interestingly, it is known that the six-state clock model transition belongs to the XY universality class in three spatial dimensions, with the sixfold anisotropy perturbation being irrelevant at the critical point [42–45].

Thus, at $T = 0$ and in a 2D triangular lattice, a valley-polarized nematic quantum critical point (QCP) should share the same universality class as a QCP associated with a hypothetical XY electronic nematic order parameter, that is completely decoupled from the lattice degrees of freedom [46]. In other words, a 2D 6-state clock model exhibits a continuous phase transition at $T = 0$, that is described by a $(2 + 1)$D Ginzburg-Landau theory of an O(2) order parameter, with a $Z_6$ anisotropic term — the latter is irrelevant in the renormalization group (RG) sense. In fact, the sixfold anisotropy term is *dangerously irrelevant* [42], as it becomes a relevant perturbation inside the ordered state [43, 47–51]. As a result, the valley-polarized nematic phase displays a pseudo-Goldstone mode, i.e., a would-be Goldstone mode with a small gap, that satisfies certain scaling properties as the QCP is approached [52].

In this paper, we explore the properties of the valley-polarized nematic state in twisted moiré systems, and, more broadly, in a generic metal. We start from a phenomenological SU(4) model, relevant for TBG, which is unstable towards intra-valley nematicity. We show that, depending on the inter-valley coupling, the resulting nematic order can be a "standard" nematic phase, which only breaks threefold rotational symmetry, or the valley-polarized nematic phase, which also breaks twofold and time-reversal symmetries. By employing group-theory techniques, we show that the onset of valley-polarized nematicity triggers in-plane orbital magnetism, as well as standard nematicity and different types of order in the valley degrees of freedom. The $Z_6$ symmetry of the valley-polarized nematic order parameter is translated as six different orientations for the in-plane magnetic moments. Moving beyond phenomenology, we use the six-band tight-binding model for TBG of Ref. [53] to investigate how valley-polarized nematic order impacts the electronic spectrum. Because the combined $C_{2z}\mathcal{T}$ symmetry is preserved, the Dirac cones remain intact, albeit displaced from the $K$ point. Moreover, band degeneracies associated with the valley degrees of freedom are lifted, and the Fermi surface acquires characteristic distortion patterns.

We next study the electronic properties of the valley-polarized nematic phase at $T = 0$, when a putative quantum critical point is crossed. To make our results more widely applicable, we consider the case of a generic metal with a simple circular Fermi surface. First, we show that the phase fluctuations inside the valley-polarized phase couple directly to the electronic density. Then, using a two-patch model [19–22, 54, 55], we show that the electronic self-energy $\Sigma$ displays, along the hot regions of the Fermi surface and above a characteristic energy $\Omega^*$, the same NFL behaviour as in the case of an "ideal" XY nematic order parameter [8, 12], i.e. $\Sigma(\nu_n) \sim i\,|\nu_n|^{2/3}$, where $\nu_n$ is the fermionic Matsubara frequency. Below $\Omega^*$, however, we find that $\Sigma(\nu_n) \sim i\,\nu_n$, and Fermi liquid (FL) behaviour is restored. Moreover, the bosonic self-energy, describing the phase fluctuations, acquires an overdamped dynamics due to the coupling to the fermions.

Exploiting the scaling properties of the six-state clock model, we argue that this NFL-to-FL crossover energy scale $\Omega^*$, which is directly related to the dangerously irrelevant variable $\lambda$ of the six-state clock model via $\Omega^* \sim \lambda^{3/2}$, is expected to be much smaller than the other energy scales of the problem. As a result, we expect NFL behaviour to be realized over an extended range of energies. We discuss possible experimental manifestations of this effect at finite temperatures, and the extension of this mechanism to the case of *spin-polarized nematic order* [32], which has been proposed to occur in moiré systems with higher-order Van Hove singularities [56, 57]. We also discuss possible limitations of the results arising from the simplified form assumed for the Fermi surface.

The paper is organized as follows: Sec. II presents a phenomenological description of valley-polarized nematic order in TBG, as well as its manifestations on the thermodynamic and electronic properties. Sec. III introduces the bosonic and fermionic actions that describe the system inside the valley-polarized nematic state. Sec. IV describes the results for the electronic self-energy, obtained from both the Hertz-Millis theory and the patch methods, focussing on the onset of an NFL behaviour. In Sec. V, we discuss the implications of our results for the observation of NFL behaviour in different types of systems.

## II. VALLEY-POLARIZED NEMATIC ORDER IN TBG

### A. Phenomenological model

In TBG, the existence of electron-electron interactions larger than the narrow bandwidth of the moiré bands [58, 59] enables the emergence of a wide range of possible ordered states involving the spin, valley, and sublattice degrees of freedom [30, 60–81]. Here, we start by considering a model for TBG that has U(1) valley symmetry. Together with the symmetry under independent spin rotations on the two valleys, the model has an emergent SU(4) symmetry, and has been widely studied previously [66, 72, 77, 80, 82, 83]. Within the valley subspace $a$, we assume that the system has an instability towards a nematic phase, i.e. an intra-valley Pomeranchuk instability that breaks the $C_{3z}$ rotational symmetry. Indeed, several models for TBG have found proximity to a nematic instability [30, 57, 71, 77, 78, 84–87]. Note here that $a = +, -$ refers to the moiré valley. Hereinafter, we assume that the

valleys are exchanged by a $C_{2x}$ rotation. Let the intra-valley nematic order associated with valley $a$ be described by the two-component order parameter $\boldsymbol{\varphi}_a = (\varphi_{a,1},\, \varphi_{a,2})$ that transforms as the $\left(d_{x^2-y^2}, d_{xy}\right)$-wave form factors.

A single valley does not have $C_{2z}$ symmetry or $C_{2x}$ symmetry (but it does have $C_{2y}$ symmetry); it is the full system, with two valleys, that has the symmetries of the $D_6$ space group. A $C_{2z}$ rotation (or, equivalently, a $C_{2x}$ rotation) exchanges valleys + and −. Time-reversal $\mathcal{T}$ has the same effect. If the valleys were completely decoupled, the nematic free energy would be

$$F_0\left(\boldsymbol{\varphi}_+, \boldsymbol{\varphi}_-\right) = r_0\left(\boldsymbol{\varphi}_+^2 + \boldsymbol{\varphi}_-^2\right) + \mathcal{O}\left(\boldsymbol{\varphi}_a^3\right), \tag{1}$$

to leading order. However, since independent spatial rotations on the two valleys are not a symmetry of the system, there must be a quadratic term coupling the two intra-valley nematic order parameters, of the form

$$\bar{F} = \kappa\left(\boldsymbol{\varphi}_+ \cdot \boldsymbol{\varphi}_-\right) = \frac{\kappa}{2}\, \boldsymbol{\varphi}_a \cdot \tau^x_{aa'}\, \boldsymbol{\varphi}_{a'}\,, \tag{2}$$

where $\tau^i$ is a Pauli matrix in valley space. This term is invariant under both $C_{2z}$ and $\mathcal{T}$, as it remains the same upon exchange of the two valleys. Moreover, it is invariant under $C_{3z}$, since it is quadratic in the nematic order parameters. It is important to note that $C_{3z}$ must be considered as a global threefold rotation, equal in both valleys.

Minimizing the full quadratic free energy, we find two possible orders depending on the sign of $\kappa$, which ultimately can only be determined from microscopic considerations. For $\kappa < 0$, the resulting order parameter

$$\tilde{\boldsymbol{\Phi}} = \boldsymbol{\varphi}_+ + \boldsymbol{\varphi}_- \tag{3}$$

is valley-independent. It has the same transformation properties as $\boldsymbol{\varphi}_a$ under $C_{3z}$, and it is even under both $C_{2z}$ and $\mathcal{T}$. As a result, it must transform as the $E_2^+$ irreducible representation of $D_6$ (the "+" superscript indicates that it is even under time-reversal). This is the usual nematic order parameter, which belongs to the three-state Potts/clock model universality class. Indeed, parametrizing $\tilde{\boldsymbol{\Phi}} = \tilde{\Phi}_0\left(\cos\tilde{\alpha},\, \sin\tilde{\alpha}\right)$, one finds a free-energy

$$\tilde{F} = r\,\tilde{\Phi}_0^2 - 2\,\lambda\,\tilde{\Phi}_0^3\cos(3\tilde{\alpha}) + u\,\tilde{\Phi}_0^4\,, \tag{4}$$

corresponding to the three-state Potts or clock model [16, 30]. For $\kappa > 0$, the resulting order parameter

$$\boldsymbol{\Phi} = \boldsymbol{\varphi}_+ - \boldsymbol{\varphi}_- \tag{5}$$

is valley-polarized. The key difference between this phase and the earlier one is that $\boldsymbol{\Phi}$ is odd under both $C_{2z}$ and $\mathcal{T}$, while retaining the same transformation properties under $C_{3z}$. Therefore, $\boldsymbol{\Phi}$ must transform as the $E_1^-$ irreducible representation of $D_6$, with the "−" superscript indicating that it is odd under time-reversal. This is the valley-polarized nematic order parameter, first identified in Ref. [30]. The full free-energy for $\boldsymbol{\Phi}$ can be obtained from its symmetry properties, rather than starting from the uncoupled free energies in Eq. (1). Parametrizing $\boldsymbol{\Phi} = \Phi_0\left(\cos\alpha,\, \sin\alpha\right)$, one finds the following free-energy expansion [30]:

$$F = r\,\Phi_0^2 + u\,\Phi_0^4 - 2\,\lambda\,\Phi_0^6\cos(6\alpha)\,. \tag{6}$$

The $\lambda$-term in Eq. (6) is the lowest-order term that lowers the symmetry of $\boldsymbol{\Phi}$ from O(2) to $Z_6$. As a result, the action corresponds to a six-state clock model. Indeed, minimization of the action with respect to the phase $\alpha$ leads to six different minima, corresponding to (1) $\alpha = \frac{\pi}{3}\,n$ for $\lambda > 0$; and (2) $\alpha = \frac{\pi}{3}\left(n + \frac{1}{2}\right)$ for $\lambda < 0$ (with $n = 0, \ldots, 5$). At finite temperatures, the 2D six-state clock model undergoes two Kosterlitz-Thouless transitions: the first one signals quasi-long-range order of the phase $\alpha$, whereas the second one marks the onset of discrete symmetry-breaking and long-range order [41].

### B. Manifestations of the valley-polarized phase

The onset of valley-polarized order leads to several observable consequences. First, we note that the in-plane magnetic moment $\mathbf{m} = (m_x,\, m_y)$ also transforms as $E_1^-$. Therefore the following linear-in-$\Phi$ free-energy coupling term is allowed:

$$\delta F_1 \sim \mathbf{m}\cdot\boldsymbol{\Phi}\,. \tag{7}$$

This implies that valley-polarized nematic order necessarily triggers in-plane magnetic moments — see also Ref. [88] for the case of in-plane magnetic moments induced by hetero-strain. These moments are directed towards the angles $\alpha$ that minimize the sixth-order term $\Phi_0^6\cos(6\alpha)$ of the nematic free energy. Because the system has SU(2) spin-rotational invariance, $\mathbf{m}$ must be manifested as an in-plane orbital angular magnetic moment. Therefore, valley-polarized nematic order provides a mechanism for in-plane orbital magnetism, which is complementary to previous models for out-of-plane orbital magnetism.

There are additional manifestations coming from higher-order terms of the free energy. Valley-polarized nematic order $\boldsymbol{\Phi}$ also induces the "usual" nematic order $\tilde{\boldsymbol{\Phi}}$ via the quadratic-linear coupling

$$\delta F_2 \sim \left(\Phi_1^2 - \Phi_2^2\right)\tilde{\Phi}_1 - 2\Phi_1\,\Phi_2\,\tilde{\Phi}_2 = \Phi_0^2\,\tilde{\Phi}_0\cos\left(2\alpha + \tilde{\alpha}\right). \tag{8}$$

Moreover, $\boldsymbol{\Phi}$ also induces either the order parameter $\eta$, which transforms as $B_2^-$, or the order parameter $\tilde{\eta}$, which transforms as $B_1^-$. Both $\eta$ and $\tilde{\eta}$ are even under $C_{3z}$, but odd under $C_{2z}$ and $\mathcal{T}$. The only difference is that $\eta$ is odd under $C_{2x}$ and even under $C_{2y}$, whereas $\tilde{\eta}$ is odd under $C_{2y}$ and even under $C_{2x}$. We find the following cubic-linear terms are allowed:

$$\begin{aligned}
\delta F_3^{(1)} &\sim \left(3\,\Phi_1^2\,\Phi_2 - \Phi_2^3\right)\eta = \Phi_0^3\,\eta\,\sin(3\alpha)\,,\\
\delta F_3^{(2)} &\sim \left(\Phi_1^3 - 3\,\Phi_1\,\Phi_2^2\right)\tilde{\eta} = \Phi_0^3\,\tilde{\eta}\,\cos(3\alpha)\,.
\end{aligned} \tag{9}$$

Since

$$\cos^2(3\alpha) = \frac{1+\cos(6\alpha)}{2} \text{ and } \sin^2(3\alpha) = \frac{1-\cos(6\alpha)}{2}\,, \tag{10}$$

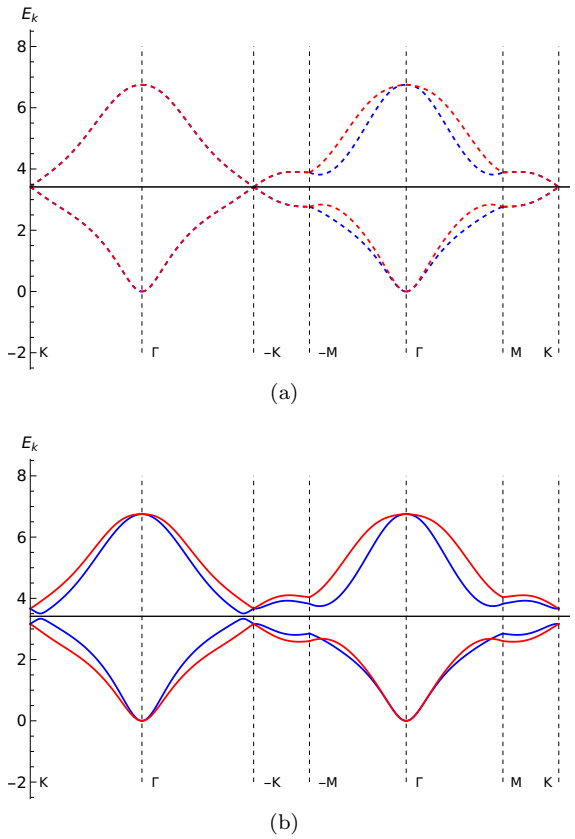



FIG. 1. Band structure along the high symmetry directions of the moiré Brillouin zone, for the (almost) flat bands of TBG. This is numerically computed from the six-orbital model of Ref. [53], without [panel (a); dashed lines] and with [panel (b); solid lines] valley-polarized nematic ordering. Red and blue lines refer to the two valleys. The parameters used are the same as in Ref. [53], and we have chosen $\Phi_0 = 0.01\, t_\kappa$ and $\alpha = 0$ for the ordered state. The energy values shown are in meV.

we conclude that, if the coefficient $\lambda$ of the $\Phi_0^6 \cos(6\alpha)$ term is positive [implying $\cos(6\alpha) = +1$], $\tilde{\eta}$ is induced. Otherwise, if $\lambda$ is negative [implying $\cos(6\alpha) = -1$], $\eta$ is induced. Physically, $\eta$ can be interpreted as a valley charge polarization $\eta = \rho_+ - \rho_-$, where $\rho_a$ is the charge at valley $a$. That is because $C_{2x}$ also switches valleys 1 and 2. On the other hand, $C_{2y}$ does not involve valley switching and is therefore an intra-valley type of order.

### C. Impact of the valley-polarized order on the electronic spectrum

To investigate how the valley-polarized nematic order parameter impacts the electronic excitations of TBG, we use the six-band model of Ref. [53]. This model, which has valley $U(1)$ symmetry, is described in terms of the electronic operator

$$\Psi_a^\dagger(\mathbf{k}) = (p_{a,\mathbf{k}z}^\dagger, p_{a,\mathbf{k}+}^\dagger, p_{a,\mathbf{k}-}^\dagger, s_{1a,\mathbf{k}}^\dagger, s_{2a,\mathbf{k}}^\dagger, s_{3a,\mathbf{k}}^\dagger) \qquad (11)$$

for valley $a$, which contains the $p$-orbitals $(p_z, p_+, p_-)$ living on the sites of the triangular moiré superlattice, and $s$-orbitals $(s_1, s_2, s_3)$ living on the sites of the related Kagome lattice. The non-interacting Hamiltonian is given by

$$\mathcal{H}_0 = \sum_{\mathbf{k}} \begin{pmatrix} \Psi_+^\dagger & \Psi_-^\dagger \end{pmatrix} \begin{pmatrix} H_{\mathbf{k}} & 0 \\ 0 & U_{C_{2z}}^\dagger H_{\mathbf{k}} U_{C_{2z}} \end{pmatrix} \begin{pmatrix} \Psi_+ \\ \Psi_- \end{pmatrix}, \qquad (12)$$

where the $6 \times 6$ matrices $H_{\mathbf{k}}$ and $U_{C_{2z}}$ are those defined in Refs. [16, 53]. Generalizing the results of Ref. [16], the coupling to the valley-polarized nematic order parameter $\Phi$ can be conveniently parametrized in the $(p_+, p_-)$ subspace as

$$\mathcal{H}_\Phi = \sum_{\mathbf{k}} \begin{pmatrix} \Psi_+^\dagger & \Psi_-^\dagger \end{pmatrix} \begin{pmatrix} H_\Phi & 0 \\ 0 & -H_\Phi \end{pmatrix} \begin{pmatrix} \Psi_+ \\ \Psi_- \end{pmatrix}, \qquad (13)$$

with the block-diagonal matrix $H_\Phi = (0_{\mathbf{1}}, \delta H_\Phi, 0_{\mathbf{3}})$, where

$$\delta H_\Phi = \begin{pmatrix} 0 & \Phi_0\, e^{-i\,\alpha} \\ \Phi_0\, e^{i\,\alpha} & 0 \end{pmatrix}. \qquad (14)$$

In Fig. 1, we show the electronic structure of the moiré flat bands in the normal state (a) and in the valley-polarized nematic state (b) parametrized by $\Phi_0 = 0.01\, t_\kappa$ and $\alpha = 0$, where $t_\kappa = 27$ meV is a hopping parameter of $H_{\mathbf{k}}$ [53]. The high-symmetry points $\Gamma$, $K$, and $M$ all refer to the moiré Brillouin zone. The main effect of the nematic valley-polarized order on the flat bands is to lift the valley-degeneracy along high-symmetry directions. Although $C_{2z}$ and $\mathcal{T}$ symmetries are broken, the combined symmetry $C_{2z}\mathcal{T}$ remains intact in the valley-polarized nematic phase. As a result, the Dirac cones of the non-interacting band structure are not gapped, but instead move away from the $K$ points, similarly to the case of standard (i.e. non-polarized) nematic order. We also note that the Van Hove singularity at the $M$ point is also altered by valley-polarized nematicity.

The Fermi surfaces corresponding to each of the six nematic valley-polarized domains, described by $\alpha = n\,\pi/3$ with $n = 0, 1, \ldots, 5$, are shown in Fig. 2. The Fermi surface of the normal state is also shown in Fig. 2(a) for comparison (dashed lines). In the ordered state, the Fermi surfaces arising from different valleys are distorted in different ways, resulting in a less symmetric Fermi surface as compared with the previously studied case of standard (i.e. non-polarized) nematicity. While the Fermi surface is no longer invariant under out-of-plane two-fold or three-fold rotations, it remains invariant under a two-fold rotation with respect to an in-plane axis. Moreover, the Fermi surfaces from different valleys continue to cross even in the presence of valley-polarized nematic order.

## III. PSEUDO-GOLDSTONE MODES IN THE VALLEY-POLARIZED NEMATIC PHASE AT ZERO TEMPERATURE

In the previous section, we studied the general properties of valley-polarized nematic order in TBG. We now proceed to investigate the unique properties of the valley-polarized nematic state at $T = 0$ in a metallic system, which stem from the emergence of a pseudo-Goldstone mode. As a first step, we extend the free energy in Eq. (6) to a proper

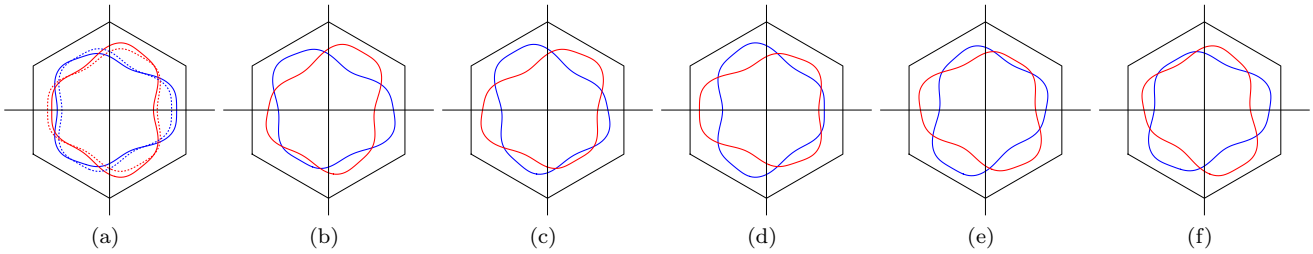



FIG. 2. Fermi surfaces in the valley-polarized nematic state arising from the flat bands of TBG: The parameters are the same as those in Fig. 1, except for $\alpha$, which here assumes the values $n\,\pi/3$, with $n \in [0, 5]$. Panels (a) to (f) correspond to $n = 0$ to $n = 5$, respectively, indicating the six different domains that minimize the free energy. In panel (a), the Fermi surfaces in the absence of valley-polarized nematic order are shown by the dashed lines. Red and blue lines refer to the two different valleys.

action. To simplify the notation, we introduce the complex valley-polarized nematic order parameter $\Phi = \Phi_1 - i\,\Phi_2 = \Phi_0\, e^{i\,\alpha}$. We obtain (see also Ref. [30])

$$S = \frac{1}{2}\int d^2x\, d\tau \left[\frac{1}{c^2}\,|\partial_\tau \Phi|^2 + |\partial_{\mathbf{x}}\Phi|^2 + r\,|\Phi|^2 + u\,|\Phi|^4 - \lambda\left(\Phi^6 + \Phi^{*6}\right)\right]. \qquad (15)$$

Here, $\mathbf{x}$ denotes the position vector, $\tau$ denotes the imaginary time, and $c$ denotes the bosonic velocity. The quadratic coefficient $r$ tunes the system towards a putative quantum critical point (QCP) at $r = r_c$, and the quartic coefficient $u > 0$. Because of the anisotropic $\lambda$-term, the action corresponds to a six-state clock model. As explained in Sec. II, at finite temperatures, the behaviour of this model is the same as that of the two-dimensional (2D) six-state clock model. This model is known [41] to first undergo a Kosterlitz-Thouless transition towards a state where the phase $\alpha$ has quasi-long-range order (like in the 2D XY model), which is then followed by another Kosterlitz-Thouless transition towards a state where $\alpha$ acquires a long-range order, pointing along one of the six directions that minimize the sixth-order term.

At $T = 0$, near a valley-polarized nematic QCP, the bosonic model in Eq. (15) maps onto the three-dimensional (3D) six-state clock model [44, 52]. One of the peculiarities of this well-studied model is that the $\lambda$-term is a *dangerously irrelevant perturbation* [43, 47–51]. Indeed, the scaling dimension $y$ associated with the $\lambda$ coefficient is negative; while an $\epsilon$-expansion around the upper critical dimension $d_c = 4$ gives $y = -2 - \epsilon$ [43], recent Monte Carlo simulations report $y \approx -2.55$ for the classical 3D six-state clock model [48, 51].

To understand what happens inside the ordered state, we use the parametrization $\Phi = |\Phi_0|\, e^{i\,\alpha}$, with fixed $|\Phi_0|$, and consider the action for the phase variable $\alpha$ only, as shown below:

$$S_\alpha = \frac{1}{2}\int d^2x\, d\tau \left[\rho_\tau\,|\partial_\tau \alpha|^2 + \rho_x\,|\partial_{\mathbf{x}}\alpha|^2 - 2\,\lambda\,|\Phi_0|^6\,\cos(6\alpha)\right]. \qquad (16)$$

Here, $\rho_x$ and $\rho_\tau$ are generalized stiffness coefficients. Expanding around one of the minima of the last term (let us call it $\alpha_0$) gives

$$S_\alpha = \frac{1}{2}\int d^2x\, d\tau \left[\rho_\tau|\partial_\tau\,\tilde{\alpha}|^2 + \rho_x\,|\partial_{\mathbf{x}}\tilde{\alpha}|^2 + 36\,|\lambda|\,|\Phi_0|^6\,\tilde{\alpha}^2\right], \qquad (17)$$

where a constant term is dropped, and $\tilde{\alpha} \equiv \alpha - \alpha_0$. It is clear that the $\lambda$-term, regardless of its sign, introduces a mass for the phase variable. Thus, while the $\lambda$-term is irrelevant at the critical point, which is described by the XY fixed point, it is relevant inside the ordered phase, which is described by a $Z_6$ fixed point, rather than the Nambu-Goldstone fixed point (that characterizes the ordered phase of the 3D XY model) [43, 51, 52].

Importantly, due to the existence of this dangerously irrelevant perturbation, there are two correlation lengths in the ordered state [47–50, 52]: $\xi$ associated with the usual amplitude fluctuations of $\Phi$; and $\xi'$ associated with the crossover from continuous to discrete symmetry-breaking of $\alpha$. Although both diverge at the critical point, they do so with different exponents $\nu$ and $\nu'$, respectively. Because $\nu' > \nu$, there is a wide range of length scales (and energies, in the $T = 0$ case) for which the ordered phase behaves as if it were an XY ordered phase. In Monte Carlo simulations, this is signalled by the emergence of a nearly-isotropic order parameter distribution [47]. More broadly, this property is expected to be manifested as a small gap in the spectrum of phase fluctuations, characteristic of a *pseudo-Goldstone mode* [89].

For simplicity of notation, in the remainder of this paper, we rescale $(\tau, \mathbf{x})$ to absorb the stiffness coefficients. Moreover, we set $\lambda > 0$ and choose $\alpha_0 = 0$, such that $\tilde{\alpha} = \alpha$. Defining $m^2 \equiv 36\,|\lambda|\,|\Phi_0|^6$, and taking the Fourier transform, the phase action becomes

$$S_\alpha = \frac{1}{2}\int_q \alpha(-q)\left(\omega_n^2 + \mathbf{q}^2 + m^2\right)\alpha(q), \qquad (18)$$

where $q = (\omega_n, \mathbf{q})$, $\omega_n$ is the bosonic Matsubara frequency, and $\mathbf{q}$ is the momentum. Here, we also introduced the notation $\int_q = T\sum_{\omega_n}\int \frac{d^2\mathbf{q}}{(2\pi)^2}$. At $T = 0$, $T\sum_{\omega_n} \to \int \frac{d\omega_n}{2\pi}$; although the subscript $n$ is not necessary, since $\omega_n$ is a continuous variable, we will keep it to distinguish it from the real-axis frequency.

Having defined the free bosonic action, we now consider the electronic degrees of freedom. While our work is motivated by the properties of TBG, in this section we choose a simple, generic band dispersion to shed light on the general properties of the $T = 0$ valley-polarized nematic state. As we will argue later, this formalism also allows us to discuss the case of a spin-polarized nematic state. The free fermionic action is given by:

$$S_f = \int_k \sum_{a=1,2} \psi_a^\dagger(k) \left[ i\,\nu_n + \varepsilon_a(\mathbf{k}) \right] \psi_a(k)\,, \tag{19}$$

where $k = (\nu_n, \mathbf{k})$, $a$ is the valley index, and $\nu_n$ is the fermionic Matsubara frequency. The electronic dispersion $\varepsilon_a(\mathbf{k})$ of valley $a$ could, in principle, be derived from the tight-binding model of Eq. (12); for our purposes, however, we keep it generic. In this single-band version of the model, the valley-polarized nematic order parameter couples to the fermionic degrees of freedom as described by the action [30]

$$S_{bf} = \gamma_0 \int_{k,q} \sum_{a=1,2} (-1)^{a+1}\, \psi_a^\dagger(k+q)\, \psi_a(k) \times \left[ \frac{\Phi(q) + \Phi^*(q)}{2} \cos(2\theta_k) - \frac{\Phi(q) - \Phi^*(q)}{2\,i} \sin(2\theta_k) \right]. \tag{20}$$

Here, $\gamma_0$ is a coupling constant, and $\tan\theta_k = k_y/k_x$. Writing $\Phi = |\Phi_0|\, e^{i\,\alpha}$, we obtain the coupling between the phase variable and the electronic operators inside the valley-polarized nematic state with constant $|\Phi_0|$. As before, we set $\alpha_0 = 0$, and expand around the minimum, to obtain

$$S_{\alpha f} = \gamma \int_{k,q} \sum_{a=1,2} (-1)^{a+1}\, \psi_a^\dagger(k+q)\, \psi_a(k) \times \left[ \cos(2\theta_k)\, (2\pi)^3\, \delta^3(k-q) - \alpha(q)\, \sin(2\theta_k) \right]. \tag{21}$$

where $\gamma \equiv \gamma_0\, |\Phi_0|$. The first term in the last line shows that long-range order induces opposite nematic distortions in the Fermi surfaces with opposite valley quantum numbers. The second term shows that the phase mode couples to the charge density directly via a Yukawa-like coupling. As discussed in Ref. [11], this is an allowed coupling when the generator of the broken symmetry does not commute with the momentum operator.

## IV. NON-FERMI LIQUID TO FERMI LIQUID CROSSOVER

### A. The patch model

Our goal is to derive the properties of the electronic degrees of freedom in the valley-polarized nematic ordered phase, which requires the computation of the electronic self-energy. To do that in a controlled manner, we employ the patch method discussed in Ref. [19–22, 54, 55]. This relies on the fact that fermions from different patches of a Fermi surface interact with a massless order parameter with largely disjoint sets of momenta, and that the inter-patch coupling is small in the low-energy limit, unless the tangent vectors at the patches are locally parallel or anti-parallel. Thus, the advantage of this emergent locality in momentum space is that we can now decompose the full theory into a sum of two-patch theories, where each two-patch theory describes electronic excitations near two antipodal points, interacting with the order parameter boson with momentum along the local tangent. This formalism has been successfully used in computing the universal properties and scalings for various NFL systems, such as the Ising-nematic QCP [19–23, 90], the Fulde-Ferrell-Larkin-Ovchinnikov (FFLO) QCP [54], and a critical Fermi surface interacting with transverse gauge field(s) [55]. The only scenario that breaks this locality in momentum space is the presence of short-ranged four-fermion interactions in the pairing channel [24, 25].

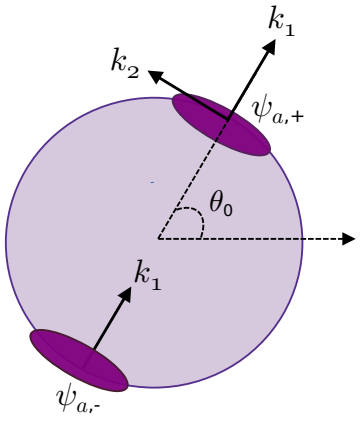



FIG. 3. Illustration of the patch model: $\psi_{a,+}$ denotes the fermions located at the upper light purple patch, centered at an angle $\theta = \theta_0$ with respect to the global coordinate system for a circular Fermi surface of valley quantum number $a$ (denoted by the dark purple ring). $\psi_{a,-}$ denotes the fermions in the lower light purple patch, centred at the antipodal point $\theta = \pi + \theta_0$, whose tangential momenta are parallel to those at $\theta_0$. Although we show here the patch construction for a circular Fermi surface for the sake of simplicity, this can be applied to any Fermi surface of a generic shape, as long as it is locally convex at each point.

For our case of the valley-polarized nematic order parameter, we consider two antipodal patches on a simplified Fermi surface, which is locally convex at each point. The antipodal patches feature opposite Fermi velocities, and couple with the bosonic field [20–22, 54]. Here, we choose a patch centred at $\theta_k = \theta_0$, and construct our coordinate system with its origin at $\theta_0$. As explained above, we must also include the fermions at the antipodal patch with $\theta_k = \pi + \theta_0$. We denote the fermions living in the two antipodal patches as $\psi_+$ and $\psi_-$, as illustrated in Fig. 3. We note that the coupling constant remains the same for the fermions in the two antipodal points.

Expanding the spectrum around the Fermi surface patches up to an effective parabolic dispersion, and using Eqs. (18), (19), and (21), we thus obtain the effective field

theory in the patch construction as

$$
\begin{aligned}
S_{\rm tot} &= S_f + S_\alpha + S_{\alpha f}\,, \text{where} \\
S_f &= \int_k \sum_{\substack{s=\pm \\ a=1,2}} \psi^\dagger_{a,s}(k)\Big(i\,\nu_n + s\,k_1 + \frac{k_2^2}{2\,k_F}\Big)\psi_{a,s}(k)\,, \\
S_\alpha &= \frac{1}{2}\int_q \alpha(-q)\left(\omega_n^2 + q_1^2 + q_2^2 + m^2\right)\alpha(q)\,, \\
S_{\alpha f} &= \sum_{\substack{s=\pm \\ a=1,2}} (-1)^a \int_{k,q} \psi^\dagger_{a,s}(k+q)\Big[\gamma\sin(2\theta_0)\,\alpha(q) \\
&\qquad\qquad - \gamma\cos(2\theta_0)\Big]\psi_{a,s}(k)\,. \qquad (22)
\end{aligned}
$$

Here, for simplicity, we have assumed that the Fermi surface is convex, and has the same shape for both the valley quantum numbers. We will discuss the impact of these approximations later in this section. Note that the fermionic momenta are expanded about the Fermi momentum $k_F$ at the origin of the coordinate system of that patch. In our notation, shown in Fig. 3, $k_1$ is directed along the local Fermi momentum, whereas $k_2$ is perpendicular to it (or tangential to the Fermi surface). Note that the local curvature of the Fermi surface is given by $1/k_F$. Furthermore, $\psi_{a,+}$ ($\psi_{a,-}$) is the right-moving (left-moving) fermion with valley index $a$, whose Fermi velocity along the $k_1$ direction is positive (negative).

Following the patch approach used in Refs. [20–22, 55], we rewrite the fermionic fields in terms of the two-component spinor $\Psi$, where

$$
\begin{aligned}
\Psi^T(k) &= \Big(\psi_{1,+}(k) \quad \psi_{2,+}(k) \quad \psi^\dagger_{1,-}(-k) \quad \psi^\dagger_{2,-}(-k)\Big)\,, \\
\bar\Psi(k) &= \Psi^\dagger(k)\,\sigma_2\otimes\tau_0\,. \qquad (23)
\end{aligned}
$$

Here, $\sigma_i$ (with $i = 1,2,3$) denotes the $i^{\rm th}$ Pauli matrix acting on the patch space (consisting of the two antipodal patches), whereas $\tau_i$ is the $i^{\rm th}$ Pauli matrix acting on valley space (not to be confused with imaginary time $\tau$, which has no subscript). We use the symbols $\sigma_0$ and $\tau_0$ to denote the corresponding $2\times 2$ identity matrices. In this notation, the full patch action $S_{\rm tot} = S_f + S_\alpha + S_{\alpha f}$ consists of

$$
\begin{aligned}
S_f &= \int_k \bar\Psi^\dagger(k)\left[i\left(\sigma_2\,\nu_n + \sigma_1\,\delta_k\right)\otimes\tau_0\right]\Psi(k)\,, \quad S_\alpha = \frac{1}{2}\int_q \alpha(-q)\left(\omega_n^2 + q_1^2 + q_2^2 + m^2\right)\alpha(q)\,, \\
S_{\alpha f} &= \gamma\int_{k,q}\bar\Psi(k+q)\left[(2\pi)^3\,\delta^3(k-q)\,\cos(2\theta_0)\,\sigma_2 - i\,\sin(2\theta_0)\,\alpha(q)\,\sigma_1\right]\otimes\tau_3\,\Psi(k)\,, \quad \delta_k = k_1 + \frac{k_2^2}{2\,k_F}\,. \qquad (24)
\end{aligned}
$$

For convenience, we have included the valley-dependent Fermi surface distortion $\gamma\cos(2\theta_0)$ in the interaction action. The form of $S_f$ is such that it appears as if the fermionic energy disperses only in one effective direction near the Fermi surface. Hence, according to the formulation of the patch model in Refs. [20–22, 54], the $(2+1)$-dimensional fermions can be viewed as if they were a $(1+1)$-dimensional "Dirac" fermion, with the momentum along the Fermi surface interpreted as a continuous flavor.

From Eq. (24), the bare fermionic propagator can be readily obtained as

$$
G_0(k) = -i\,\frac{\sigma_2\,\nu_n + \sigma_1\,\delta_k}{\nu_n^2 + \delta_k^2}\otimes\tau_0\,. \qquad (25)
$$

We note that the strength of the coupling constant between the bosons and the fermions, given by $\gamma\,\sin(2\theta_k)$, depends on the value of $\theta_k$. For the patch centered at $\theta_k = \theta_0$, the leading order term from the loop integrals can be well-estimated by assuming $\theta = \theta_0$ for the entire patch, as long as $\sin(2\theta_0) \neq 0$. However, for $\sin(2\theta_0) = 0$, we need to go beyond the leading order terms (which are zero), while performing the loop integrals. The patches centered around $\theta_k = \theta_0$, with $\sin(2\theta_0) \sim 0$, are the so-called "cold spots"; we will refer to the other patches as belonging to the "hot regions" of the Fermi surface.

### B. Electronic self-energy

We first compute the one-loop bosonic self-energy $\Pi_1$, which takes the form:

$$
\begin{aligned}
\Pi_1(q) &= -\,(i\,\gamma)^2\int\frac{d^3k}{(2\,\pi)^3}\left[\sin^2(2\theta_0) + \frac{4\,k_2^2\cos(4\theta_0)}{k_F^2} + \frac{2\,k_2\sin(4\theta_0)}{k_F}\right]{\rm Tr}\left[\sigma_1\,G_0(k+q)\,\sigma_1 G_0(k)\right] \\
&= -\frac{\gamma^2\sin^2(2\theta_0)\,k_F\,|\omega_n|}{\pi\,|q_2|} + \frac{2\,\gamma^2\sin(4\theta_0)\,k_F\,\delta_q\,|\omega_n|}{\pi\,q_2\,|q_2|} + \frac{4\,\gamma^2\cos(4\theta_0)\,k_F\,|\omega_n|\left[\pi\left(q_0^2 - \delta_q^2\right) - 2|q_0|\,|q_2|\right]}{\pi^2\,|q_2|^3}\,. \qquad (26)
\end{aligned}
$$

This result is obtained by considering a patch centered around $\theta_k = \theta_0$ and then expanding $\sin^2(2\theta_0 + 2\,k_2/k_F)$ in inverse powers of $k_F$. In the limits $\frac{|\omega_n|}{|q_2|} \ll 1$, $k_F \gg |\mathbf{q}|$,

and $|\mathbf{q}| \to \mathbf{0}$, we have, to leading order

$$\Pi_1(q)\Big|_{\rm hr} = -\frac{|\omega_n|}{|q_2|}\frac{\gamma^2 \sin^2(2\theta_0)\, k_F}{\pi}, \tag{27}$$

as long as $\sin(2\theta_0) \neq 0$ (i.e., in the hot regions). For the cold spots, the leading-order term is given by

$$\Pi_1(q)\Big|_{\rm cs} = -\frac{8\,\gamma^2 \cos(4\theta_0)\, k_F}{\pi^2}\frac{\omega_n^2}{q_2^2}, \tag{28}$$

Here, the subscript "hr" ("cs") denotes hot regions (cold spots). A similar result was previously obtained in Refs. [8, 10] using a different approach, and for the case of an XY nematic order parameter (see also [91]). Therefore, we conclude that the pseudo-Goldstone mode in the valley-polarized nematic phase is overdamped in the hot regions.

We can now define the dressed bosonic propagator, which includes the one-loop bosonic self-energy, as

$$D_1(q) = \frac{1}{q^2 + m^2 - \Pi_1(q)}\,. \tag{29}$$

The one-loop fermionic self-energy $\Sigma_1(k)$ can then be expressed in terms of $\tilde{\Sigma}$, defined as

$$\begin{aligned}\tilde{\Sigma}(k) &\equiv \Sigma_1(k) - \gamma\, \cos(2\,\theta_0)\, \sigma_2 \otimes \tau_3 \\ &= -\gamma^2 \sin^2(2\theta_0) \int_q (\sigma_1 \otimes \tau_3)\, G_0(k+q)\, (\sigma_1 \otimes \tau_3)\, D_1(-q)\,,\end{aligned} \tag{30}$$

where we use the notation $q = (\omega_{n'}, \mathbf{q})$. In order to be able to perform the integrals, we will neglect the $q_1^2$ and $\omega_{n'}^2$ contributions in the bosonic propagator, which are anyway irrelevant in the RG sense [20, 21]. This is justified because the contributions to the integral are dominated by $q_1 \sim \nu_n$, $\omega_{n'} \sim \nu_n$, and $q_2 \sim |\nu_n|^{1/3}$, and we are interested in the small $|\nu_n|$ limit (where $\nu_n$ is the external fermionic Matsubara frequency). In the limit $m \to 0$, we can obtain analytical expressions for $\tilde{\Sigma}(k)$ as follows:

$$\begin{aligned}&\tilde{\Sigma}(k)\Big|_{{\rm hr}, m\to 0} \\ &= -\gamma^2 \sin^2(2\theta_0) \int_q (\sigma_1 \otimes \tau_3)\, G_0(k+q)\, (\sigma_1 \otimes \tau_3)\, D_1(-q) \\ &= -\frac{i\,[\gamma \sin(2\theta_0)]^{4/3}\, {\rm sgn}(\nu_n)\, |\nu_n|^{2/3}}{2\sqrt{3}\,\pi^{2/3}\, k_F^{1/3}}\, \sigma_2 \otimes \tau_0\,,\end{aligned} \tag{31}$$

$$\begin{aligned}&\tilde{\Sigma}(k)\Big|_{{\rm cs}, m\to 0} \\ &= -\frac{i\,\gamma^{3/2} \cos^{\frac{3}{4}}(4\theta_0)\, {\rm sgn}(\nu_n)\, |\nu_n|^{1/2}\, k_2^2}{2^{1/4}\sqrt{\pi}\, k_F^{9/4}}\, \sigma_2 \otimes \tau_0\,.\end{aligned} \tag{32}$$

The one-loop corrected self-energy is then given by $G^{-1}(k) = G_0^{-1}(k) - \Sigma_1(k)$. The frequency dependence of $\tilde{\Sigma}$ in the hot regions, in the limit $m \to 0$, corresponds to an NFL behaviour, since the fermionic lifetime has a sub-linear dependence on frequency, implying the absence of well-defined quasiparticles. The same $|\nu_n|^{2/3}$ dependence on the frequency was found in the case of an ideal XY nematic in Refs. [8, 12].

However, for the valley-polarized nematic state, $m$ is not zero in the ordered state, as it is proportional to the square root of the dangerously irrelevant variable $\lambda$ in the bosonic action. The limit of large $m$ is straightforward to obtain, and gives an FL-correction to the electronic Green's function, because

$$\begin{aligned}&\tilde{\Sigma}(k)\Big|_{{\rm hr}, m \gg \left[\frac{3\sqrt{3}\,\gamma^2\, k_F \sin^2(2\theta_0)\,|\nu_n|}{2\,\pi}\right]^{1/3}} \\ &= -\frac{\left(2 + 2^{2/3}\right)\gamma^2 \sin^2(2\theta_0)}{8\,\pi\, m}\, i\,\nu_n\, \sigma_2 \otimes \tau_0\,.\end{aligned} \tag{33}$$

From Eqs. (25), (29), and (30), we find that the crossover from NFL to FL behaviour occurs when $m^2 > -\Pi_1(q)$, i.e., $m^2 > \frac{|\omega_{n'}|\,\gamma^2 k_F \sin^2(2\theta_0)}{\pi\, q_2}$ in the one-loop corrected bosonic propagator $D_1(q)$ inside the integral. In that situation, the dominant contribution to the integral over $q_2$ comes from $q_2 \sim m$. On the other hand, considering the fermionic propagator contribution to the integrand, the dominant contribution comes from $\omega_{n'} \sim \nu_n$ for the $\omega_{n'}$-integral. Hence, the relevant crossover scale for the fermionic frequency $\nu_n$ is approximately $\Omega^* = \frac{m^3}{\gamma^2\, k_F \sin^2(2\theta_0)}$. Because $m^2 \sim \lambda$, it follows that $\Omega^* \sim \lambda^{3/2}$.

It is therefore expected that, for finite $m$, above the characteristic energy scale $\Omega^*$, the self-energy displays NFL behaviour, captured by $\tilde{\Sigma} \sim i\,{\rm sgn}(\nu_n)\,|\nu_n|^{2/3}$. For low enough energies, such that $|\nu_n| \ll \Omega^*$, the regular FL behaviour with $\tilde{\Sigma} \sim i\,\nu_n$ should be recovered. The crucial point is that, because $\Omega^*$ depends on the dangerously irrelevant coupling constant $\lambda$, it is expected to be a small energy scale. This point will be discussed in more depth in the next section. To proceed, it is convenient to write the complete expression for $\tilde{\Sigma} = \bar{\Sigma} \times (\sigma_2 \otimes \tau_0)$ for the case of an arbitrary $m$:

$$\begin{aligned}&i\,\bar{\Sigma}(k)\Big|_{\rm hr} \\ &= -\int d\tilde{\omega}_{n'} \frac{m^3\, {\rm sgn}\left(\tilde{\nu}_n + \tilde{\omega}_{n'}\right)}{4\,\pi^2} \sum_{j=1}^{3} \frac{\zeta_j(\tilde{\omega}_{n'}) \ln\left(-\zeta_j(\tilde{\omega}_{n'})\right)}{m^2 + 3\,\zeta_j^2(\tilde{\omega}_{n'})}\,,\end{aligned} \tag{34}$$

where $\tilde{\nu}_n \equiv \nu_n/\Omega^*$, $\tilde{\omega}_{n'} \equiv \omega_{n'}/\Omega^*$, and $\zeta_j$ is the $j^{\rm th}$ root of the cubic-in-$q_2$ polynomial $\pi\, q_2 \left(q_2^2 + m^2\right) + m^3\, k_F\, |\tilde{\omega}_{n'}|$.

To confirm that indeed $\Omega^*$ is the energy scale associated with the crossover from NFL to FL behaviour, we have solved the integral in Eq. (34) numerically to obtain the self-energy for arbitrary $m$. As shown in Fig. 4, $\Omega^*$ separates the two asymptotes for the self-energy $\tilde{\Sigma}$: (1) NFL, given by Eq. (31), and present for $\nu_n \gg \Omega^*$; (2) FL, given by Eq. (33), and present for $\nu_n \ll \Omega^*$.

As explained in the beginning of this section, here we have considered the simplified case of two identical convex Fermi surfaces for the two valleys. This not only makes the analytic calculations more tractable, but also allows us to extend the results for more general cases beyond TBG. This includes, for instance, the case where $a$ is not a valley quantum number, but a spin quantum number, which we will discuss in more detail in Sec. V.

Considering the Fermi surfaces for TBG obtained from the tight-binding model and shown in Fig. 2, it is clear that

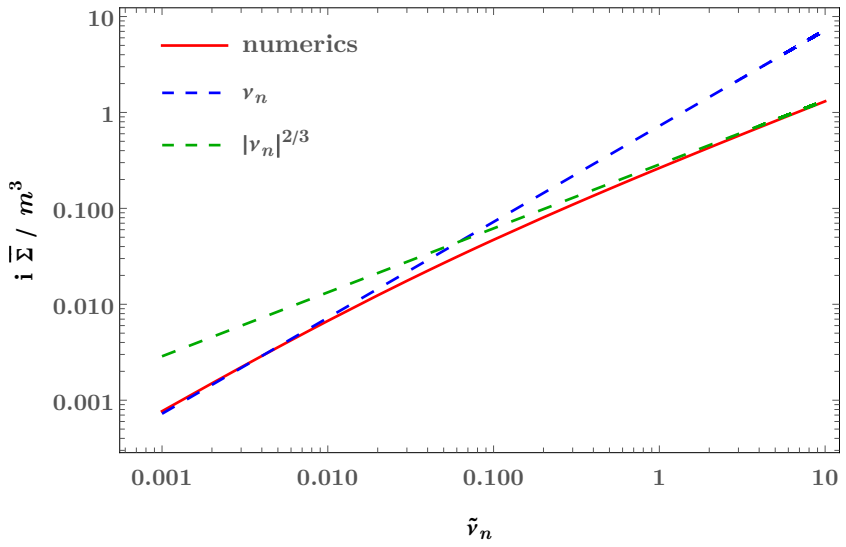



FIG. 4. Fermionic self-energy $i\,\bar{\Sigma}(\nu_n)/m^3$ as a function of the scaled Matsubara frequency $\tilde{\nu}_n = \nu_n/\Omega^*$, obtained from the numerical integration of Eq. (34) by setting $m = 0.1$ and $k_F = 100$. The dashed lines correspond to the frequency dependencies obtained from the asymptotic results in Eq. (31) [ i.e., $i\,\bar{\Sigma}\,(\nu_n) \sim |\nu_n|^{2/3}$] and in Eq. (33) [i.e., $i\,\bar{\Sigma}\,(\nu_n) \sim \nu_n$].

they each have a lower three-fold (rather than continuous) rotational symmetry in the disordered state. One of the consequences is that the two patches in the patch model are no longer related by inversion, at least not within the same valley Fermi surface. Another consequence is that the Fermi surface can have points that are locally concave and not convex. The latter is an important assumption of the patch model construction of Ref. [20, 55], which we have implemented here. The impact of these two effects on the self-energy behaviour at moderate frequencies is an interesting question beyond the scope of this work, which deserves further investigation. While we still expect an FL-to-NFL crossover, the particular frequency dependence of the self-energy, in the regime where the pseudo-Goldstone mode appears gapless, may be different from what has been discussed in this section.

### C. Hertz-Millis approach

We note that the same general results obtained above also follow from the usual (but uncontrolled) Hertz-Millis approach [92]. It turns out that the action in Eq. (21) is analogous to the widely studied case of a metallic Ising-nematic QCP, and hence the results are well known (see, for example, Refs. [17, 19, 93, 94]). Linearizing the dispersion near the Fermi level, the one-loop bosonic self-energy is given by

$$\bar{\Pi}_1(q) = -\gamma^2\, k_F \int_{-\infty}^{\infty} \frac{d\nu_{n'}}{2\,\pi} \int_{-\infty}^{\infty} \frac{dk_\perp}{2\,\pi} \int_0^{2\pi} \frac{d\theta_k}{2\,\pi} \frac{\sin^2(2\theta_k)}{(i\,\nu_{n'} - k_\perp)\,[i\,(\nu_{n'} + \omega_n) - \{k_\perp + |\mathbf{q}|\cos(\theta_k - \theta_q)\}]}\,. \tag{35}$$

A straightforward computation gives the final expression:

$$\bar{\Pi}_1(q) \propto -\gamma^2 \sin^2(2\theta_q)\, \frac{|\omega_n|}{|\mathbf{q}|}\,. \tag{36}$$

Thus, we obtain the dynamical critical exponent $z = 3$ for the bosons [except at the cold spots, where the coupling constant $\sin^2(2\theta_q)$ vanishes]. This is the usual Hertz-Millis result for a bosonic QCP in a metal, whose ordered state has zero wavevector [92]. Most importantly, it gives an NFL fermionic self-energy $\bar{\Sigma}_1 \propto i\,|\nu_n|^{2/3}$ if the bosonic mass $m = 0$, and the usual FL expression with $\bar{\Sigma}_1 \propto i\,\nu_n$ for $m \neq 0$ (see, for example, Ref. [92]).

As mentioned above, these results are analogous to those for an Ising-nematic QCP in a metal. The difference here is that the QCP is approached from the ordered state, rather than from the disordered state. More importantly, in our case, it is not the gap in the amplitude fluctuations, but the small mass of the pseudo-Goldstone mode associated with phase fluctuations that restores the FL behaviour, as one moves away from the QCP. These phase fluctuations, in turn, couple to the fermionic degrees of freedom via a Yukawa-like coupling, rather than a gradient-like coupling (typical for phonons). The key point is that because the pseudo-Goldstone behaviour arises from a dangerously irrelevant variable, its relevant critical exponent $\xi'$ is different from the critical exponent $\xi$ associated with the amplitude fluctuations.

## V. DISCUSSION AND CONCLUSIONS

Our calculations with the patch model, assuming convex Fermi surfaces with antipodal patches with parallel tangent vectors, show that $\Omega^* \sim \lambda^{3/2}$. In other words, the energy scale $\Omega^*$, associated with the NFL-to-FL crossover, is directly related to the dangerously irrelevant coupling constant $\lambda$ of the six-state clock model. This has important consequences for the energy range in which the NFL is expected to be observed in realistic settings. In the classical 3D $Z_6$ clock model, it is known that the dangerously irrelevant variable $\lambda$ introduces a new length scale $\xi'$ in the ordered phase [47–50]. It is only beyond this length scale that the discrete nature of the broken symmetry is manifested; below it, the system essentially behaves as if it were in the ordered state of the XY model. Like the standard correlation length $\xi$, which is associated with fluctuations of the amplitude mode, $\xi'$ also diverges upon approaching the QCP from the ordered state. However, its critical exponent $\nu'$ is larger than the XY critical exponent $\nu$, implying that $\xi' \gg \xi$ as the QCP is approached. As a result, there is a wide range of length scales for which the ordered state is similar to that of the XY model.

Applying these results to our quantum model, we therefore expect a wide energy range for which the fermionic self-energy displays the same behaviour as fermions coupled to a hypothetical XY nematic order parameter, i.e., the NFL behaviour $\Sigma \sim i\,\mathrm{sgn}(\nu_n)\,|\nu_n|^{2/3}$. Thus, the actual crossover energy scale $\Omega^*$ should be very small compared with other energy scales of the problem. This analysis suggests that the valley-polarized nematic state in a triangular lattice is a promising candidate to display the strange metallic behaviour predicted originally for the "ideal" (i.e., hypothetically uncoupled from the lattice) XY nematic phase in the square lattice [8].

It is important to point out a caveat with this analysis. Although the aforementioned critical behaviour of the $Z_6$ clock model has been verified by Monte Carlo simulations, for both the 3D classical case and the 2D quantum case [52], the impact of the coupling to the fermions remains to be determined. The results of our patch model calculations for the bosonic self-energy show the emergence of Landau damping in the dynamics of the phase fluctuations, which is expected to change the universality class of the QCP — and the value of the exponent $\nu$ — from 3D XY to Gaussian, due to the reduction of the upper critical dimension. The impact of Landau damping on the crossover exponent $\nu'$ is a topic that deserves further investigation, particularly since even in the purely bosonic case, there are different proposals for the scaling expression for $\nu'$ (see Ref. [52] and references therein).

We also emphasize the fact that our results have been derived for $T = 0$. Experimentally, however, NFL behaviour is often probed at nonzero temperatures. It is therefore important to determine whether the NFL behaviour of the self-energy persists at a small nonzero temperature. At first sight, this may seem difficult, since in the classical 2D $Z_6$ clock model, the $\lambda$-term is a relevant perturbation. In fact, as discussed in Sec. III, the system in 2D displays two Kosterlitz-Thouless transitions, with crossover temperature scales of $T_{\mathrm{KT},1}$ and $T_{\mathrm{KT},2}$, with $Z_6$ symmetry-breaking setting in below $T_{\mathrm{KT},2}$ [41]. However, a more in-depth analysis, as outlined in Ref. [50], indicates that as the QCP is approached, a new crossover temperature $T^* < T_{\mathrm{KT},2}$ emerges, below which the ordered state is governed by the QCP (rather than the thermal transition). Not surprisingly, the emergence of $T^*$ is rooted on the existence of the dangerously irrelevant perturbation along the $T = 0$ axis. Therefore, as long as $\Omega^* < T^*$, the NFL behaviour is expected to be manifested at nonzero temperatures. Whether and how it is manifested in resistivity measurements, which are the primary tools to probe NFL behaviour, require further investigations beyond the scope of this paper. One of the issues involved is that the quasiparticle inverse lifetime, which can be obtained directly from the self-energy, is different from the actual transport scattering rate, which is hardly affected by small-angle scattering processes [91, 93, 95].

An obvious candidate to display a valley-polarized nematic state is twisted bilayer graphene and, more broadly, twisted moiré systems. Experimentally, as we showed in this paper, a valley-polarized nematic state would be manifested primarily as in-plane orbital ferromagnetism, breaking threefold rotation, twofold rotation, and time-reversal symmetries. While several experiments have reported evidence for out-of-plane orbital ferromagnetism [37–40], it remains to be seen whether there are regions in the phase diagram where the magnetic moments point in-plane [88]. An important property of the valley-polarized nematic state is that the Dirac points remain protected, albeit displaced from the $K$ point, since the combined $C_{2z}\mathcal{T}$ operation remains a symmetry of the system.

A somewhat related type of order, which has also been proposed to be realized in twisted bilayer graphene and other systems with higher-order Van Hove singularities [56, 57], is the *spin-polarized nematic order* [31–33]. It is described by an order parameter of the form $\overrightarrow{\varphi} = (\overrightarrow{\varphi}_1, \overrightarrow{\varphi}_2)$, where the indices denote the two $d$-wave components associated with the irreducible representation $E_2$ of the point group $\mathrm{D}_6$. The arrows denote that these quantities transform as vectors in spin space. The main difference between $\overrightarrow{\varphi}$ and the valley-polarized nematic state is that the spin-polarized nematic state does not break the $C_{2z}$ symmetry. It is therefore interesting to ask whether our results would also apply for this phase. The main issue is that $\overrightarrow{\varphi}$ is not described by a six-state clock model, since an additional quartic term is present in the action (see Ref. [56]), which goes as:

$$S_{\vec{\varphi}} \sim (\vec{\varphi}_1 \cdot \vec{\varphi}_2)^2 - |\vec{\varphi}_1|^2\,|\vec{\varphi}_2|^2 \,. \tag{37}$$

However, if spin-orbit coupling is present in such a way that $\overrightarrow{\varphi}$ becomes polarized along the $z$-axis, this additional term vanishes. The resulting order parameter $\varphi^z = (\varphi_1^z, \varphi_2^z)$ transforms as the $E_2^-$ irreducible representation, and its corresponding action is the same as Eq. (15), i.e., a six-state clock model. Moreover, the coupling to the fermions has the same form as in Eq. (20), with $a$ now denoting the spin projection, rather than the valley quantum number. Consequently, we also expect an NFL-to-FL crossover inside the Ising spin-polarized nematic state.

In summary, we presented a phenomenological model for the emergence of valley-polarized nematic order in twisted

moiré systems, which is manifested as in-plane orbital ferromagnetism. More broadly, we showed that when a metallic system undergoes a quantum phase transition to a valley-polarized nematic state, the electronic self-energy at $T = 0$ in the ordered state displays a crossover from the FL behaviour (at very low energies) to NFL behaviour (at low-to-moderate energies). This phenomenon is a consequence of the six-state-clock ($Z_6$) symmetry of the valley-polarized nematic order parameter, which implies the existence of a pseudo-Goldstone mode in the ordered state, and of a Yukawa-like coupling between the phase mode and the itinerant electron density. The existence of the pseudo-Goldstone mode arises, despite the discrete nature of the broken symmetry, because the anisotropic $\lambda$-term in the bosonic action [cf. Eq. (15)], which lowers the continuous O(2) symmetry to $Z_6$, is a dangerously irrelevant perturbation. Our results thus provide an interesting route to realize NFL behaviour in twisted moiré systems.

## ACKNOWLEDGMENTS

We thank A. Chakraborty, S.-S. Lee, A. Sandvik, and C. Xu for fruitful discussions. RMF was supported by the U. S. Department of Energy, Office of Science, Basic Energy Sciences, Materials Sciences and Engineering Division, under Award No. DE-SC0020045.

[1] Y. Jiang, X. Lai, K. Watanabe, T. Taniguchi, K. Haule, J. Mao, and E. Y. Andrei, Charge order and broken rotational symmetry in magic-angle twisted bilayer graphene, Nature **573**, 91–95 (2019).

[2] A. Kerelsky, L. J. McGilly, D. M. Kennes, L. Xian, M. Yankowitz, S. Chen, K. Watanabe, T. Taniguchi, J. Hone, C. Dean, A. Rubio, and A. N. Pasupathy, Maximized electron interactions at the magic angle in twisted bilayer graphene, Nature **572**, 95 (2019).

[3] Y. Choi, J. Kemmer, Y. Peng, A. Thomson, H. Arora, R. Polski, Y. Zhang, H. Ren, J. Alicea, G. Refael, F. von Oppen, K. Watanabe, T. Taniguchi, and S. Nadj-Perge, Electronic correlations in twisted bilayer graphene near the magic angle, Nature Physics **15**, 1174 (2019).

[4] Y. Cao, D. Rodan-Legrain, J. M. Park, N. F. Q. Yuan, K. Watanabe, T. Taniguchi, R. M. Fernandes, L. Fu, and P. Jarillo-Herrero, Nematicity and competing orders in superconducting magic-angle graphene, Science **372**, 264 (2021).

[5] C. Rubio-Verdú, S. Turkel, Y. Song, L. Klebl, R. Samajdar, M. S. Scheurer, J. W. F. Venderbos, K. Watanabe, T. Taniguchi, H. Ochoa, L. Xian, D. M. Kennes, R. M. Fernandes, Á. Rubio, and A. N. Pasupathy, Moiré nematic phase in twisted double bilayer graphene, Nature Physics 10.1038/s41567-021-01438-2 (2021).

[6] R. Samajdar, M. S. Scheurer, S. Turkel, C. Rubio-Verdú, A. N. Pasupathy, J. W. F. Venderbos, and R. M. Fernandes, Electric-field-tunable electronic nematic order in twisted double-bilayer graphene, 2D Materials **8**, 034005 (2021).

[7] S. A. Kivelson, E. Fradkin, and V. J. Emery, Electronic liquid-crystal phases of a doped Mott insulator, Nature **393**, 550 (1998).

[8] V. Oganesyan, S. A. Kivelson, and E. Fradkin, Quantum theory of a nematic Fermi fluid, Phys. Rev. B **64**, 195109 (2001).

[9] Y. B. Kim and H.-Y. Kee, Pairing instability in a nematic Fermi liquid, Journal of Physics: Condensed Matter **16**, 3139 (2004).

[10] M. Zacharias, P. Wölfle, and M. Garst, Multiscale quantum criticality: Pomeranchuk instability in isotropic metals, Phys. Rev. B **80**, 165116 (2009).

[11] H. Watanabe and A. Vishwanath, Criterion for stability of goldstone modes and Fermi liquid behavior in a metal with broken symmetry, Proceedings of the National Academy of Sciences **111**, 16314 (2014).

[12] M. Garst and A. V. Chubukov, Electron self-energy near a nematic quantum critical point, Phys. Rev. B **81**, 235105 (2010).

[13] E. Fradkin, S. A. Kivelson, M. J. Lawler, J. P. Eisenstein, and A. P. Mackenzie, Nematic Fermi fluids in condensed matter physics, Annual Review of Condensed Matter Physics **1**, 153 (2010).

[14] R. M. Fernandes, A. V. Chubukov, and J. Schmalian, What drives nematic order in iron-based superconductors?, Nature Physics **10**, 97–104 (2014).

[15] M. Hecker and J. Schmalian, Vestigial nematic order and superconductivity in the doped topological insulator $Cu_xBi_2Se_3$, npj Quantum Materials **3**, 26 (2018).

[16] R. M. Fernandes and J. W. F. Venderbos, Nematicity with a twist: Rotational symmetry breaking in a moiré superlattice, Science Advances **6**, eaba8834 (2020).

[17] W. Metzner, D. Rohe, and S. Andergassen, Soft Fermi surfaces and breakdown of Fermi-liquid behavior, Phys. Rev. Lett. **91**, 066402 (2003).

[18] J. Rech, C. Pépin, and A. V. Chubukov, Quantum critical behavior in itinerant electron systems: Eliashberg theory and instability of a ferromagnetic quantum critical point, Phys. Rev. B **74**, 195126 (2006).

[19] M. A. Metlitski and S. Sachdev, Quantum phase transitions of metals in two spatial dimensions. i. Ising-nematic order, Phys. Rev. B **82**, 075127 (2010).

[20] D. Dalidovich and S.-S. Lee, Perturbative non-Fermi liquids from dimensional regularization, Phys. Rev. B **88**, 245106 (2013).

[21] I. Mandal and S.-S. Lee, Ultraviolet/infrared mixing in non-Fermi liquids, Phys. Rev. B **92**, 035141 (2015).

[22] I. Mandal, UV/IR mixing in non-Fermi liquids: higher-loop corrections in different energy ranges, European Physical Journal B **89**, 278 (2016).

[23] A. Eberlein, I. Mandal, and S. Sachdev, Hyperscaling violation at the Ising-nematic quantum critical point in two-dimensional metals, Phys. Rev. B **94**, 045133 (2016).

[24] M. A. Metlitski, D. F. Mross, S. Sachdev, and T. Senthil, Cooper pairing in non-Fermi liquids, Phys. Rev. B **91**, 115111 (2015).

[25] I. Mandal, Superconducting instability in non-Fermi liquids, Phys. Rev. B **94**, 115138 (2016).

[26] S. Lederer, Y. Schattner, E. Berg, and S. A. Kivelson, Enhancement of superconductivity near a nematic quantum critical point, Phys. Rev. Lett. **114**, 097001 (2015).

[27] A. Klein and A. Chubukov, Superconductivity near a nematic quantum critical point: Interplay between hot and lukewarm regions, Phys. Rev. B **98**, 220501 (2018).

[28] E. Y. Andrei and A. H. MacDonald, Graphene bilayers with

a twist, Nature Materials **19**, 1265 (2020).
[29] L. Balents, C. R. Dean, D. K. Efetov, and A. F. Young, Superconductivity and strong correlations in moiré flat bands, Nature Physics **16**, 725 (2020).
[30] Y. Xu, X.-C. Wu, C.-M. Jian, and C. Xu, Orbital order and possible non-Fermi liquid in moiré systems, Phys. Rev. B **101**, 205426 (2020).
[31] S. A. Kivelson, I. P. Bindloss, E. Fradkin, V. Oganesyan, J. M. Tranquada, A. Kapitulnik, and C. Howald, How to detect fluctuating stripes in the high-temperature superconductors, Rev. Mod. Phys. **75**, 1201 (2003).
[32] C. Wu, K. Sun, E. Fradkin, and S.-C. Zhang, Fermi liquid instabilities in the spin channel, Phys. Rev. B **75**, 115103 (2007).
[33] M. H. Fischer and E.-A. Kim, Mean-field analysis of intra-unit-cell order in the Emery model of the $CuO_2$ plane, Phys. Rev. B **84**, 144502 (2011).
[34] Y. Cao, V. Fatemi, A. Demir, S. Fang, S. L. Tomarken, J. Y. Luo, J. D. Sanchez-Yamagishi, K. Watanabe, T. Taniguchi, E. Kaxiras, R. C. Ashoori, and P. Jarillo-Herrero, Correlated insulator behaviour at half-filling in magic-angle graphene superlattices, Nature **556**, 80–84 (2018).
[35] Y. Cao, V. Fatemi, S. Fang, K. Watanabe, T. Taniguchi, E. Kaxiras, and P. Jarillo-Herrero, Unconventional superconductivity in magic-angle graphene superlattices, Nature **556**, 43 (2018).
[36] M. Yankowitz, S. Chen, H. Polshyn, Y. Zhang, K. Watanabe, T. Taniguchi, D. Graf, A. F. Young, and C. R. Dean, Tuning superconductivity in twisted bilayer graphene, Science **363**, 1059 (2019).
[37] X. Lu, P. Stepanov, W. Yang, M. Xie, M. A. Aamir, I. Das, C. Urgell, K. Watanabe, T. Taniguchi, G. Zhang, A. Bachtold, A. H. MacDonald, and D. K. Efetov, Superconductors, orbital magnets and correlated states in magic-angle bilayer graphene, Nature **574**, 653–657 (2019).
[38] A. L. Sharpe, E. J. Fox, A. W. Barnard, J. Finney, K. Watanabe, T. Taniguchi, M. A. Kastner, and D. Goldhaber-Gordon, Emergent ferromagnetism near three-quarters filling in twisted bilayer graphene, Science **365**, 605 (2019).
[39] M. Serlin, C. L. Tschirhart, H. Polshyn, Y. Zhang, J. Zhu, K. Watanabe, T. Taniguchi, L. Balents, and A. F. Young, Intrinsic quantized anomalous hall effect in a moiré heterostructure, Science **367**, 900–903 (2020).
[40] C. L. Tschirhart, M. Serlin, H. Polshyn, A. Shragai, Z. Xia, J. Zhu, Y. Zhang, K. Watanabe, T. Taniguchi, M. E. Huber, and A. F. Young, Imaging orbital ferromagnetism in a moiré chern insulator, Science **372**, 1323 (2021).
[41] J. V. José, L. P. Kadanoff, S. Kirkpatrick, and D. R. Nelson, Renormalization, vortices, and symmetry-breaking perturbations in the two-dimensional planar model, Phys. Rev. B **16**, 1217 (1977).
[42] D. J. Amit and L. Peliti, On dangerous irrelevant operators, Annals of Physics **140**, 207 (1982).
[43] M. Oshikawa, Ordered phase and scaling in $Z_n$ models and the three-state antiferromagnetic Potts model in three dimensions, Phys. Rev. B **61**, 3430 (2000).
[44] J. Hove and A. Sudbø, Criticality versus q in the $(2+1)$-dimensional $Z_q$ clock model, Phys. Rev. E **68**, 046107 (2003).
[45] F. Fucito and G. Parisi, On the range of validity of the $6-\varepsilon$ expansion for percolation, Journal of Physics A: Mathematical and General **14**, L507 (1981).
[46] K. Ishida, M. Tsujii, S. Hosoi, Y. Mizukami, S. Ishida, A. Iyo, H. Eisaki, T. Wolf, K. Grube, H. v. Löhneysen, R. M. Fernandes, and T. Shibauchi, Novel electronic nematicity in heavily hole-doped iron pnictide superconductors, Proceedings of the National Academy of Sciences **117**, 6424 (2020).
[47] J. Lou, A. W. Sandvik, and L. Balents, Emergence of U(1) symmetry in the 3D XY model with $Z_q$ anisotropy, Phys. Rev. Lett. **99**, 207203 (2007).
[48] T. Okubo, K. Oshikawa, H. Watanabe, and N. Kawashima, Scaling relation for dangerously irrelevant symmetry-breaking fields, Phys. Rev. B **91**, 174417 (2015).
[49] F. Léonard and B. Delamotte, Critical exponents can be different on the two sides of a transition: A generic mechanism, Phys. Rev. Lett. **115**, 200601 (2015).
[50] D. Podolsky, E. Shimshoni, G. Morigi, and S. Fishman, Buckling transitions and clock order of two-dimensional Coulomb crystals, Phys. Rev. X **6**, 031025 (2016).
[51] H. Shao, W. Guo, and A. W. Sandvik, Monte Carlo renormalization flows in the space of relevant and irrelevant operators: Application to three-dimensional clock models, Phys. Rev. Lett. **124**, 080602 (2020).
[52] P. Patil, H. Shao, and A. W. Sandvik, Unconventional U(1) to $Z_q$ crossover in quantum and classical $q$-state clock models, Phys. Rev. B **103**, 054418 (2021).
[53] H. C. Po, L. Zou, T. Senthil, and A. Vishwanath, Faithful tight-binding models and fragile topology of magic-angle bilayer graphene, Phys. Rev. B **99**, 195455 (2019).
[54] D. Pimenov, I. Mandal, F. Piazza, and M. Punk, Non-Fermi liquid at the FFLO quantum critical point, Phys. Rev. B **98**, 024510 (2018).
[55] I. Mandal, Critical Fermi surfaces in generic dimensions arising from transverse gauge field interactions, Phys. Rev. Research **2**, 043277 (2020).
[56] L. Classen, A. V. Chubukov, C. Honerkamp, and M. M. Scherer, Competing orders at higher-order Van Hove points, Phys. Rev. B **102**, 125141 (2020).
[57] D. V. Chichinadze, L. Classen, and A. V. Chubukov, Valley magnetism, nematicity, and density wave orders in twisted bilayer graphene, Phys. Rev. B **102**, 125120 (2020).
[58] R. Bistritzer and A. H. MacDonald, Moiré bands in twisted double-layer graphene, Proceedings of the National Academy of Sciences **108**, 12233 (2011).
[59] G. Tarnopolsky, A. J. Kruchkov, and A. Vishwanath, Origin of magic angles in twisted bilayer graphene, Phys. Rev. Lett. **122**, 106405 (2019).
[60] L. Rademaker and P. Mellado, Charge-transfer insulation in twisted bilayer graphene, Phys. Rev. B **98**, 235158 (2018).
[61] H. Isobe, N. F. Q. Yuan, and L. Fu, Unconventional superconductivity and density waves in twisted bilayer graphene, Phys. Rev. X **8**, 041041 (2018).
[62] D. M. Kennes, J. Lischner, and C. Karrasch, Strong correlations and $d+id$ superconductivity in twisted bilayer graphene, Phys. Rev. B **98**, 241407 (2018).
[63] J. W. F. Venderbos and R. M. Fernandes, Correlations and electronic order in a two-orbital honeycomb lattice model for twisted bilayer graphene, Phys. Rev. B **98**, 245103 (2018).
[64] Y. Sherkunov and J. J. Betouras, Electronic phases in twisted bilayer graphene at magic angles as a result of Van Hove singularities and interactions, Phys. Rev. B **98**, 205151 (2018).
[65] A. Thomson, S. Chatterjee, S. Sachdev, and M. S. Scheurer, Triangular antiferromagnetism on the honeycomb lattice of twisted bilayer graphene, Phys. Rev. B **98**, 075109 (2018).
[66] J. Kang and O. Vafek, Strong coupling phases of partially filled twisted bilayer graphene narrow bands, Phys. Rev. Lett. **122**, 246401 (2019).
[67] K. Seo, V. N. Kotov, and B. Uchoa, Ferromagnetic Mott state in twisted graphene bilayers at the magic angle, Phys. Rev. Lett. **122**, 246402 (2019).

[68] N. F. Q. Yuan, H. Isobe, and L. Fu, Magic of high-order van Hove singularity, Nature Communications **10**, 5769 (2019).

[69] J. M. Pizarro, M. J. Calderón, and E. Bascones, The nature of correlations in the insulating states of twisted bilayer graphene, Journal of Physics Communications **3**, 035024 (2019).

[70] W. M. H. Natori, R. Nutakki, R. G. Pereira, and E. C. Andrade, SU(4) Heisenberg model on the honeycomb lattice with exchange-frustrated perturbations: Implications for twistronics and Mott insulators, Phys. Rev. B **100**, 205131 (2019).

[71] J. Kang and O. Vafek, Non-abelian Dirac node braiding and near-degeneracy of correlated phases at odd integer filling in magic-angle twisted bilayer graphene, Phys. Rev. B **102**, 035161 (2020).

[72] N. Bultinck, E. Khalaf, S. Liu, S. Chatterjee, A. Vishwanath, and M. P. Zaletel, Ground state and hidden symmetry of magic-angle graphene at even integer filling, Phys. Rev. X **10**, 031034 (2020).

[73] M. Xie and A. H. MacDonald, Nature of the correlated insulator states in twisted bilayer graphene, Phys. Rev. Lett. **124**, 097601 (2020).

[74] T. Cea and F. Guinea, Band structure and insulating states driven by Coulomb interaction in twisted bilayer graphene, Phys. Rev. B **102**, 045107 (2020).

[75] M. Christos, S. Sachdev, and M. S. Scheurer, Superconductivity, correlated insulators, and Wess–Zumino–Witten terms in twisted bilayer graphene, Proceedings of the National Academy of Sciences **117**, 29543 (2020).

[76] Y. Da Liao, J. Kang, C. N. Breiø, X. Y. Xu, H.-Q. Wu, B. M. Andersen, R. M. Fernandes, and Z. Y. Meng, Correlation-induced insulating topological phases at charge neutrality in twisted bilayer graphene, Phys. Rev. X **11**, 011014 (2021).

[77] F. Xie, A. Cowsik, Z.-D. Song, B. Lian, B. A. Bernevig, and N. Regnault, Twisted bilayer graphene. VI. An exact diagonalization study at nonzero integer filling, Phys. Rev. B **103**, 205416 (2021).

[78] E. Brillaux, D. Carpentier, A. A. Fedorenko, and L. Savary, Analytical renormalization group approach to competing orders at charge neutrality in twisted bilayer graphene, Phys. Rev. Research **4**, 033168 (2022).

[79] I. Mandal, J. Yao, and E. J. Mueller, Correlated insulators in twisted bilayer graphene, Phys. Rev. B **103**, 125127 (2021).

[80] D. V. Chichinadze, L. Classen, Y. Wang, and A. V. Chubukov, SU(4) symmetry in twisted bilayer graphene: An itinerant perspective, Phys. Rev. Lett. **128**, 227601 (2022).

[81] Z.-D. Song and B. A. Bernevig, Magic-angle twisted bilayer graphene as a topological heavy fermion problem, Phys. Rev. Lett. **129**, 047601 (2022).

[82] O. Vafek and J. Kang, Renormalization group study of hidden symmetry in twisted bilayer graphene with Coulomb interactions, Phys. Rev. Lett. **125**, 257602 (2020).

[83] Y. Wang, J. Kang, and R. M. Fernandes, Topological and nematic superconductivity mediated by ferro-su(4) fluctuations in twisted bilayer graphene, Phys. Rev. B **103**, 024506 (2021).

[84] J. F. Dodaro, S. A. Kivelson, Y. Schattner, X. Q. Sun, and C. Wang, Phases of a phenomenological model of twisted bilayer graphene, Phys. Rev. B **98**, 075154 (2018).

[85] A. O. Sboychakov, A. V. Rozhkov, A. L. Rakhmanov, and F. Nori, Spin density wave and electron nematicity in magic-angle twisted bilayer graphene, Phys. Rev. B **102**, 155142 (2020).

[86] E. Khalaf, N. Bultinck, A. Vishwanath, and M. P. Zaletel, Soft modes in magic angle twisted bilayer graphene, arXiv:2009.14827 (2020).

[87] S. Onari and H. Kontani, SU(4) valley+spin fluctuation interference mechanism for nematic order in magic-angle twisted bilayer graphene: The impact of vertex corrections, Phys. Rev. Lett. **128**, 066401 (2022).

[88] O. Antebi, A. Stern, and E. Berg, In-plane orbital magnetization as a probe for symmetry breaking in strained twisted bilayer graphene, Phys. Rev. B **105**, 104423 (2022).

[89] C. Burgess, Goldstone and pseudo-Goldstone bosons in nuclear, particle and condensed-matter physics, Physics Reports **330**, 193 (2000).

[90] I. Mandal, Zero sound and plasmon modes for non-Fermi liquids, Physics Letters A **447**, 128292 (2022).

[91] V. S. de Carvalho and R. M. Fernandes, Resistivity near a nematic quantum critical point: Impact of acoustic phonons, Phys. Rev. B **100**, 115103 (2019).

[92] H. v. Löhneysen, A. Rosch, M. Vojta, and P. Wölfle, Fermi-liquid instabilities at magnetic quantum phase transitions, Rev. Mod. Phys. **79**, 1015 (2007).

[93] S. A. Hartnoll, R. Mahajan, M. Punk, and S. Sachdev, Transport near the Ising-nematic quantum critical point of metals in two dimensions, Phys. Rev. B **89**, 155130 (2014).

[94] I. Paul and M. Garst, Lattice effects on nematic quantum criticality in metals, Phys. Rev. Lett. **118**, 227601 (2017).

[95] D. L. Maslov, V. I. Yudson, and A. V. Chubukov, Resistivity of a non-Galilean–invariant Fermi liquid near Pomeranchuk quantum criticality, Phys. Rev. Lett. **106**, 106403 (2011).